UNIVERSITÀ DEGLI STUDI DI TORINO

The definitive version is available at:
http://dx.doi.org/10.1016/j.asr.2013.05.008

truefalse

, ,
, ,

The KASCADE-Grande energy spectrum of cosmic rays and the rôle of hadronic interaction models

W.D. Apel[a], J.C. Arteaga-Velázquez[b], K. Bekk[a], M. Bertaina[c,*], J. Blümer[a,d], H. Bozdog[a], I.M. Brancus[e], E. Cantoni[c,f,1], A. Chiavassa[c], F. Cossavella[d,2], K. Daumiller[a], V. de Souza[g], F. Di Pierro[c], P. Doll[a], R. Engel[a], J. Engler[a], M. Finger[d], B. Fuchs[d], D. Fuhrmann[h,3], H.J. Gils[a], R. Glasstetter[h], C. Grupen[i], A. Haungs[a], D. Heck[a], J.R. Hörandel[j], D. Huber[d], T. Huege[a], K.-H. Kampert[h], D. Kang[d], H.O. Klages[a], K. Link[d], P. Łuczak[k], M. Ludwig[d], H.J. Mathes[a], H.J. Mayer[a], M. Melissas[d], J. Milke[a], B. Mitrica[e], C. Morello[f], J. Oehlschläger[a], S. Ostapchenko[a,4], N. Palmieri[d], M. Petcu[e], T. Pierog[a], H. Rebel[a], M. Roth[a], H. Schieler[a], S. Schoo[a], F.G. Schröder[a], O. Sima[l], G. Toma[e], G.C. Trinchero[f], H. Ulrich[a], A. Weindl[a], J. Wochele[a], M. Wommer[a], J. Zabierowski[k]

[a] *Institut für Kernphysik, KIT - Karlsruher Institut für Technologie, Postfach 3640, D-76021 Karlsruhe, Germany*

[b] *Universidad Michoacana, Instituto de Fíisica y Matemáticas, Edificio C-3, Cd. Universitaria. C. P. 58040 Morelia, Michoacan, México*

[c] *Dipartimento di Fisica, Università degli Studi di Torino, Via Giuria 1, I-10125, Torino, Italy*

[d] *Institut für Experimentelle Kernphysik, KIT - Karlsruher Institut für Technologie, Postfach 3640, D-76021 Karlsruhe, Germany*

[e] *National Institute of Physics and Nuclear Engineering, Str. Reactorului no.30, P.O.BOX MG-6, Bucharest - Magurele, Romania*

[f] *Osservatorio Astrofisico di Torino, INAF Torino, Via Osservatorio, 20 - 10025 Pino Torinese Torino, Italy*

[g] *Universidade São Paulo, Instituto de Física de São Carlos, Av. Trabalhador São-carlense, 400, 13560-970 São Carlos - SP, Brasil*

[h] *Fachbereich Physik, Universität Wuppertal, Gaussstrasse 20, D-42119 Wuppertal, Germany*

---

[*] Corresponding author

Email address: `bertaina@to.infn.it` (M. Bertaina)

[1] now at: I.N.RI.M - Istituto Nazionale di Ricerca Metrologica, Strada delle Cacce 91, 10135 Torino, Italy

[2] now at: Max-Planck-Institut für Physik, Föhringer Ring 6, D-8805 München, Germany

[3] now at: University of Duisburg-Essen, Lotharstrasse 1, D-47057 Duisburg, Germany

[4] now at: Department of Physics, Norwegian University of Science and Technology, 7491 Trondheim, Norway

Preprint submitted to Advances in Space Research *May 5, 2013*

[i]Department of Physics, Siegen University, Postfach, D-57068 Siegen, Germany
[j]Dept. of Astrophysics, Radboud University Nijmegen, P.O. Box 9010, 6500 GL Nijmegen, The Netherlands
[k]National Centre for Nuclear Research, Department of Cosmic Ray Physics, 90-950 Lodz 1, P.O.Box 447, Poland
[l]Department of Physics, University of Bucharest, Atomistilor 405, CP MG-11, RO-077125, Bucharest-Magurele, Romania

---

Abstract

Previous results obtained by KASCADE-Grande using the QGSjetII-02 hadronic interaction model have shown that the energy spectrum of cosmic rays between 10^{16} eV and 10^{18} eV exhibits a significant hardening at approximately 2×10^{16} eV and a slight but statistically significant steepening close to 10^{17} eV. Moreover, the analysis with QGSjetII-02 suggests that the break observed around 10^{17} eV is caused by the heavy component of primary cosmic rays. In this paper, we report on the results of similar analyses performed using the SIBYLL 2.1 and EPOS 1.99 hadronic interaction models to interpret the data. The present results confirm qualitatively the previous findings. However, the intensity of the all-particle spectrum, the positions of the hardening and steepening of the spectrum, as well as the relative abundance of the heavy and light mass groups depend on the hadronic interaction model used to interpret the data.

Keywords: Ultra-high energy cosmic rays, All-particle energy spectrum, Extensive Air Showers, mass composition, hadronic interaction models, KASCADE-Grande
PACS: 98.70.Sa, 95.85.Ry, 96.50.sb, 96.50.sd

---

1. Introduction

Due to the rapidly falling intensity with increasing energy, cosmic rays of energies above 10^{15} eV can be studied only indirectly by observations of extensive air showers (EAS) which are produced by the interaction of cosmic particles with nuclei of the Earth's atmosphere. The all-particle spectrum has a power-like behavior ($\propto E^{\gamma}$, $\gamma \sim -2.7$) with features known as the 'knee' around 3-5 $\times$ 10^{15} eV and 'ankle' at 4-10 $\times$ 10^{18} eV, respectively, where the spectrum shows a steepening and hardening, respectively, of the spectral index by $|\Delta\gamma| \sim 0.3$-0.4. Many astrophysical models interpreting the origin of the knee assume the existence of various breaks which depend on the charge of primary nuclei (B.Peters, 1961; J.R.Hörandel, 2004). This seems to be in agreement with previous findings of EAS-TOP and KASCADE which have shown that the knee at 3-5 $\times$ 10^{15} eV is caused by the decrease in the flux of light mass primaries (M.Aglietta et al., 2004b,a; T.Antoni et al. , 2005) and by recent findings of KASCADE-Grande (W.D.Apel et al., 2011) which indicate a bending of the heavy mass-group around 10^{17} eV. Moreover, KASCADE-Grande data indicate also the presence of a hardening of the spectrum around 2 $\times$ 10^{16} eV (W.D.Apel et al., 2012) that can be expected (C.De Donato et al., 2012) if a gap exists between the breaks of the most abundant light and heavy primaries.

The energy range between 10^{17} eV and 10^{19} eV is also very interesting as it is the region where a transition from a galactic dominated to an extra-galactic dominated composition is firmly expected (A.M.Hillas, 2005; V.Berezinsky et al. , 2006). The ankle might mark indeed such a transition. Therefore, the study of the chemical composition and of the shape of the energy spectrum in this energy range is also of great interest.

Despite the fact that ground-based observation of cosmic rays allows collecting large data samples, thereby, reducing statistical uncertainties, one has to rely on the results of simulations and the description of hadronic interactions for reconstructing the properties of the primary particles. Since the required energies and important kinematic regions of these interactions are beyond the range of collider or fixed target experiments, the interaction models used are uncertain and differ in predictions. Therefore, a cross-check of the results obtained with different interaction models will help in understanding the systematic effects of this kind.

In this paper, we present the results on the all-particle energy spectrum and mass-group separation of KASCADE-Grande data interpreted using the SIBYLL 2.1 (J.Engel et al., 1992), and EPOS 1.99 (K.Werner et al., 2006) high-energy hadronic interaction models in the CORSIKA framework (D.Heck et al., 1998), and compare them to the previous findings obtained using QGSjetII-02 (S.Ostapchenko, 2006). In this sense the present paper has to be considered as a follow-up of the analyses presented in (W.D.Apel et al., 2011) and (W.D.Apel et al., 2012). This is the reason why the technique to infer the energy spectrum and mass separation is the same as in QGSjetII-02 analyses.

In the following, the names will be abbreviated as SIBYLL, EPOS and

QGSjet, respectively. In all cases, FLUKA (G.Battistoni et al., 2006) is used to describe the low-energy interactions in the air-shower development.

2. The Technique

The technique employed to derive the all-particle energy spectrum and the abundance of 'light' and 'heavy' primaries is based on the correlation between the number of charged particles (N_{ch}) with energy $E > 3\,\mathrm{MeV}$, and muons (N_μ) with kinetic energy $E > 230\,\mathrm{MeV}$ on an event-by-event basis. The method itself has been described in detail in (M.Bertaina et al., 2011) where QGSjet simulated showers were used to analyse the data. Here, we summarize the main points and describe the results obtained using SIBYLL and EPOS.

A sample of Monte Carlo events was simulated including the full air shower development in the atmosphere, the response of the detector and its electronics as well as their uncertainties. In this way, the parameters reconstructed from the simulation are obtained in the same way as for real data. The EAS events are generated with an isotropic distribution with spectral index $\gamma = -2$, i.e. roughly one order of magnitude harder than the measured spectrum. Hence, the simulated showers are weighted to describe a softer energy spectrum with $\gamma = -3$. Sets of simulated events were produced in the energy range from $10^{15}\,\mathrm{eV}$ to $10^{18}\,\mathrm{eV}$ with high statistics and for five elements: H, He, C, Si and Fe, representative for different mass groups ($\approx$ 257,000 events per primary for SIBYLL and EPOS, $\approx$ 353,000 in case of QGSjet). Some events up to $3 \cdot 10^{18}\,\mathrm{eV}$ were also generated in order to cross-check the reconstruction behavior at the highest energies.

The relevant components of the KASCADE-Grande (W.D.Apel et al., 2010) multi-detector experiment used for the present analysis are the Grande and KASCADE arrays. Grande is formed by 37 stations of 10 m^2 scintillation detectors each, spread over an irregular grid with an average spacing of $\sim$137 m, covering an area of about $700 \times 700\,\mathrm{m}^2$ (see fig. 1) . The KASCADE array is composed of 252 detector stations ($\sim 3.2\,\mathrm{m}^2$ each) on a square grid and with 13 m spacing spread over an area of $200 \times 200\,\mathrm{m}^2$. In this analysis only the 192 stations equipped with a layer of plastic scintillator detectors shielded by iron-lead absorber (threshold of 230 MeV kinetic energy for vertical incident muons) are used. Grande stations provide the core position and angle-of-incidence, as well as the total number of charged particles in the shower (energy $E > 3\,\mathrm{MeV}$) at observation level. The values are calcu-

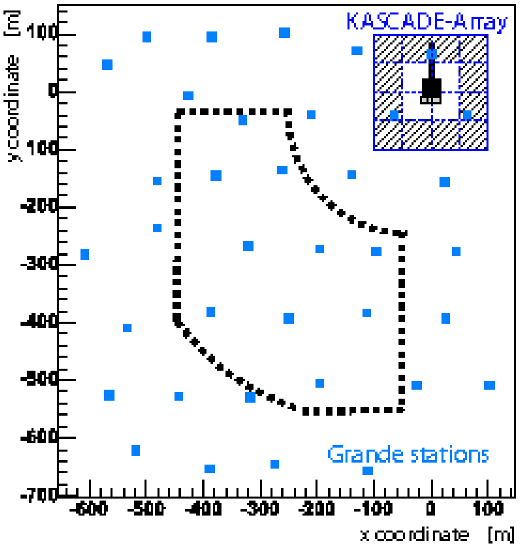

Figure 1: Layout of the KASCADE-Grande experiment: The KASCADE array and the distribution of the 37 stations of the Grande array are shown. The outer 12 clusters of the KASCADE array consist of shielded μ-detectors (cross-hatched area). The dotted line inside the Grande array shows the area of events selected for the present analysis.

lated by means of a maximum likelihood procedure comparing the measured number of particles with the one expected from a modified NKG lateral distribution function. The total number of muons is calculated using the core position determined by the Grande array and the muon densities measured by the KASCADE muon array detectors. Also in this case the total number of muons N_μ in the shower disk is derived from a maximum likelihood estimation where the lateral distribution function is based on the one proposed by (A.A.Lagutin et al., 2001). The reconstruction procedures and accuracies of KASCADE-Grande observables are described in detail in (W.D.Apel et al., 2010) and related references therein.

For the reconstruction, we restricted ourselves to events with zenith angles less than 40°. Additionally, only air showers with cores located in a central area of the KASCADE-Grande array were selected (see dotted area in fig. 1, about 0.15 km^2). With these cuts on the fiducial area, border effects are discarded and possible under- and overestimations of the muon number for events close to and far away from the center of the KASCADE array are reduced. All of these cuts were applied also to the Monte Carlo simulations to study their effects. Full efficiency for triggering and reconstruction of air-

showers is reached at a primary energy of $\approx 10^{16}$ eV.
The analysis presented here is finally based on 1173 days of data taking and the cuts on the sensitive central area and zenith angle correspond to a total acceptance of $A = 1.976 \cdot 10^9\,\mathrm{cm}^2\cdot$ sr ($0.1976\,\mathrm{km}^2\cdot$ sr), and an exposure of $N = 2.003 \cdot 10^{17}\,\mathrm{cm}^2\cdot$ sr$\cdot$ s ($0.635\,\mathrm{km}^2\cdot$ sr$\cdot$ year), respectively.
Based on Monte Carlo simulations a formula is obtained to calculate the primary energy per individual shower on the basis of the reconstructed N_{ch} and N_μ. The formula takes into account the mass sensitivity in order to minimize the composition dependence in the energy assignment, and at the same time, provides an event-by-event separation between 'light' and 'heavy' candidates. The formula is defined for 5 different zenith angle intervals ($\theta <$ 16.7, $16.7 \leq \theta < 24.0$, $24.0 \leq \theta < 29.9$, $29.9 \leq \theta < 35.1$, $35.1 \leq \theta < 40.0$ degrees) independently, to take into account shower attenuation in the atmosphere. Data are combined only at the very last stage to obtain a unique power law spectrum. The energy assignment is defined as $E = f(N_{ch}, k)$ (see equation 1), where N$_{ch}$ is the number of charged particles and the parameter k is defined through the ratio of the numbers of the N$_{ch}$ and muon (N$_\mu$) components: $k = g(N_{ch}, N_\mu)$ (see equation 2). The main aim of the k variable is to take into account the average differences in the N$_{ch}$/N$_\mu$ ratio among different primaries with similar N$_{ch}$ and the shower to shower fluctuations for events of the same primary mass:

$$\log_{10}(E[GeV]) = [a_H + (a_{Fe} - a_H) \cdot k] \cdot \log_{10}(N_{ch}) + b_H + (b_{Fe} - b_H) \cdot k \quad (1)$$

$$k = \frac{\log_{10}(N_{ch}/N_\mu) - \log_{10}(N_{ch}/N_\mu)_H}{\log_{10}(N_{ch}/N_\mu)_{Fe} - \log_{10}(N_{ch}/N_\mu)_H} \quad (2)$$

$$\log_{10}(N_{ch}/N_\mu)_{H,Fe} = c_{H,Fe} \cdot \log_{10}(N_{ch}) + d_{H,Fe}. \quad (3)$$

The k parameter is, by definition of eq. (2), a number centered around 0 for H initiated showers and 1 for Fe ones if expressed as a function of N_{ch} for Monte Carlo events. It is expected that the average values of the k paramenter for the experimental data lie between the H and Fe limits. In case this is not verified it would be a hint of some deficit of the model to describe the experimental data. Naturally, as the calibration functions differ from model to model, the same experimental event might give different values of k when SIBYLL or EPOS calibration functions are used.
A complete list of the parameters of the calibration functions for both interaction models, as well as examples of the fitting procedures for the first angular bin are reported in Appendix A. The overall performance, meant as

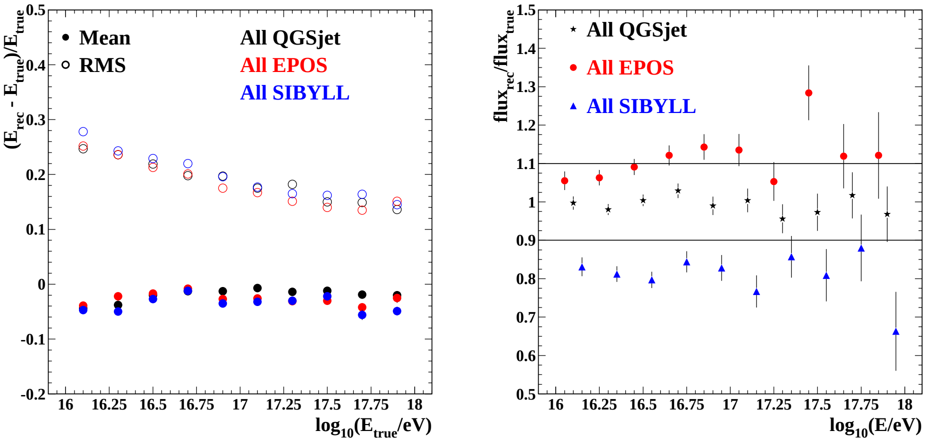

Figure 2: Left: Resolution in the energy assignment for a mixture of primaries of the 5 simulated mass groups (relative abundance of each group 20%). The full dots show the offset of the reconstructed energy E_{rec} in bins of true energy E_{true}. The open dots show the RMS of such distributions. Different colors indicate the different hadronic interaction models. Right: Ratio between the reconstructed and simulated SIBYLL, EPOS, and QGSjet spectra using QGSjet based calibration functions.

the capability of reproducing the simulated input spectra, as well as results on the energy resolution are reported as well.

Simulated events using a mixture of all primaries have been divided in bins of true energy (E_{true}) and the distributions of the relative differences between reconstructed (E_{rec}) and true energies have been created. As shown in fig.2 the RMS of such distributions (energy resolution) is $\sim 26\%$ at the energy threshold and decreases with energy, due to the lower fluctuations of the shower development and reconstruction uncertainties, becoming $< 20\%$ at the highest energies. The small offset in the mean values of the distributions at low energies is due to reproduce the flux by taking into account the effect of shower fluctuations on a steep spectrum. A similar effect exists for all hadronic interaction models.

Since the three hadronic interaction models predict for the same initial conditions a different amount of electrons and muons in the cascade, differences in the interpretation of the data will arise. As an example, the right plot of fig.2 shows the ratio between the reconstructed flux over the simulated one when SIBYLL or EPOS hadronic interaction models are used to generate air showers in the atmosphere and the energy assignment is derived using QGSjet calibration functions. In case of SIBYLL events, the flux is recon-

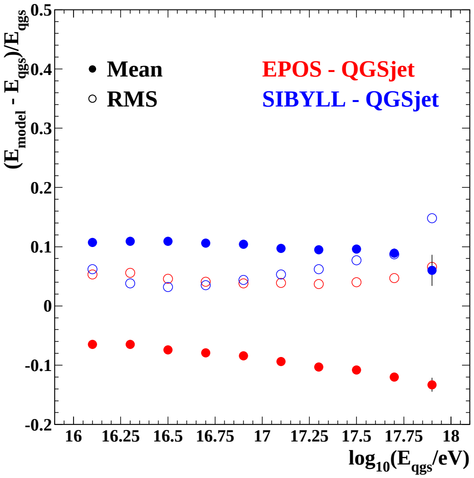

Figure 3: Difference between the energy reconstructed by SIBYLL (filled blue dots) or EPOS (filled red dots) on experimental data compared to QGSjet as a function of the energy reconstructed by QGSjet. The open dots refer to the width of the distributions in each energy bin.

structed ∼20% below the true one almost independently of energy. This indicates that the amount of electrons and muons at sea level of SIBYLL events is smaller compared to QGSjet. Moreover, the difference is essentially constant as a function of energy. On the other hand, as EPOS produces the largest number of muons of the three models, the energy assigned by the QGSjet calibration functions is higher than the energy used in the simulation of the event with EPOS, with the consequence that the reconstructed flux is higher. There are also hints that the ratio of the fluxes is not constant as a function of energy which indicates that the evolution of N$_\mu$ and N_{ch} in EPOS differs from QGSjet and SIBYLL.

As a consequence, when interpreting the same experimental event, SIBYLL is expected to assign a higher energy than QGSjet, while EPOS a lower one. This is confirmed by fig.3, which shows the average relative difference between the energy reconstructed by SIBYLL and EPOS compared to QGSjet on an event-by-event basis, for different energy bins. SIBYLL assigns on average a 10% higher energy than QGSjet at all energies, while EPOS is below by ∼6% at the threshold and by ∼12% at the highest ones, which again indicates the different behavior of EPOS compared to the other two models.

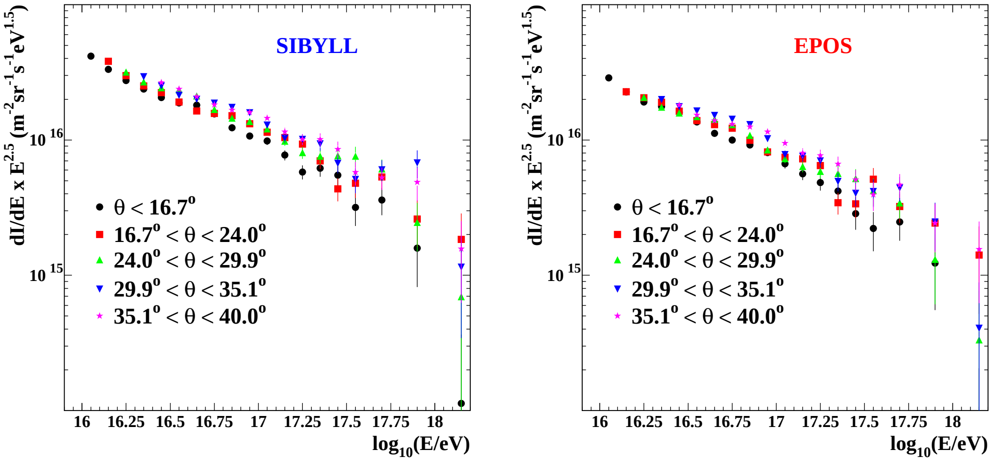

Figure 4: Reconstructed all-particle energy spectrum after unfolding for all five angular bins (left-hand panel SIBYLL, right-hand panel EPOS).

3. The energy spectrum

Applying the energy calibration functions obtained by each model to the measured data, the all-particle energy spectra for the five zenith angle bins are obtained (Fig. 4) for both SIBYLL and EPOS.

To refine the energy assignment function from the so far assumed pure power-law behavior of the $(N_{ch}, N_{ch}/N_\mu)$ and (N_{ch}, E_0) relations to a more realistic non-linear calibration, as well as to unfold bin-to-bin migrations due to shower-to-shower fluctuations, the response matrices R_{ij} for the different angular bins are constructed and applied, i.e. the spectra are unfolded (see Appendix B). Effects of this procedure on the flux are estimated to be smaller than 5% for all energy bins and therefore do not significantly change the shape of the spectra. In the following discussions on the energy spectrum we always refer to the unfolded spectra.

The spectra of the different angular bins exhibit a small systematic shift to each other, where we observe an increase in flux with increasing zenith angle. This finding was already observed with QGSjet calibration functions. This corresponds to a horizontal shift in the energy assignment, which can be explained by the fact that the real showers penetrate deeper into the atmosphere than predicted by the hadronic interaction models - a more detailed discussion can be found in (J.C.Arteaga-Velázqez et al., 2012). On the other

hand it might be related to a systematic uncertainty in the procedure to estimate the energy. For this reason we consider this comparison as a method to estimate the systematic uncertainty in the evaluation of the flux.
Different sources of uncertainty affect the all-particle energy spectrum. A detailed description is reported in (W.D.Apel et al., 2012). Here we summarize only the main points.

a) Attenuation: the average difference between the intensities obtained in the various angular bins have been used to define the systematic uncertainty associated with the angular dependence of the parameters appearing in the energy calibration functions of the different angular ranges.

b) Energy calibration and composition: the possible bias introduced in the energy spectrum by different primary compositions is checked by looking at the uncertainty in the reconstructed spectrum when a different composition is assumed. In general, such spectra are always reproduced at all energies inside 10% systematic uncertainty. An example is reported Fig.A.13 where the ratio of the reconstructed flux over the true one is obtained for the extreme cases of a composition of only 'light' (50%-50% H and He) or 'heavy' primaries (50%-50% Si and Fe).

c) Spectral slope of Monte Carlo simulations: a further source of uncertainty is the choice of a spectral slope of $\gamma = -3$ in the simulations to determine the energy calibration functions and response matrices. This is checked by constructing new response matrices based on different slopes $\gamma_1 = -2.8$ and $\gamma_2 = -3.2$ and comparing the results.

d) Reconstruction quality of N_{ch} and N_{μ}: due to the asymmetry of the location of the shower core to the muon detector.

Table 1 reports the estimated uncertainties of the cosmic ray flux for different energies for both SIBYLL and EPOS models. Those obtained by QGSjet are reported in (W.D.Apel et al., 2012).

The final all-particle spectrum of KASCADE-Grande is obtained (see Figs. 5 and 6) by combining the spectra for the individual angular ranges. Only those events are taken into account, for which the reconstructed energy is above the energy threshold for the angular bin of interest (see Fig. 4).

Table 1: Estimated uncertainties (%) of the cosmic ray flux for different energies, where only absolute values are given in case of symmetric uncertainties.

	SIBYLL			EPOS		
Source of uncertainty	10^{16} eV	10^{17} eV	10^{18} eV	10^{16} eV	10^{17} eV	10^{18} eV
intensity in different angular bins	-0/+17.6	13.2	25.5	-0/+10.8	13.0	21.6
energy calibration & composition	5.6	7.9	18.4	5.1	10.5	19.7
slope of the primary spectrum	0.3	0.2	0.2	0.1	0.2	0.3
reconstruction (core, N_{ch} & N_{μ})	1.0	0.3	5.3	0.4	0.8	5.5
total	-5.7/+18.5	15.4	31.9	-5.1/+12.0	16.7	29.7
statistical error	0.6	2.3	14.3	0.7	2.9	19.4
energy resolution (mixed compos.)	27.8	18.6	14.5	25.2	17.1	15.1

Table 2 reports the fluxes with statistical and systematic uncertainties for SIBYLL and EPOS hadronic interaction models.

In general the shape of the energy spectrum is very similar for the three models, however, a shift in flux is clearly observed. This is the consequence of the energy shift assigned on an event-by-event basis previously discussed. Looking at the residual plot (fig. 6), one observes in general an almost constant ∼25% increase in the flux of SIBYLL compared to QGSjet and a reduction of ∼10% of EPOS with respect to QGSjet at the lowest energies and slightly increasing to higher energies as expected from fig.3. This result gives an estimation on the systematic uncertainty on the experimental flux due to the hadronic interaction model used to interpret the data, and it is essentially independent of the technique used to derive the flux, namely averaging the fluxes obtained in different angular bins. The shift in the assigned energy to the data is also visible in the hardening around $\sim 2 \times 10^{16}$ eV and in the steepening around 10^{17} eV which look shifted among the models in general agreement with the energy shift. This result indicates that the features seen in the spectrum are not an artefact of the hadronic interaction model used to interpret the data but they are in the measured data. In the overlapping region, KASCADE-Grande data are compatible inside the systematic uncertainties with KASCADE data interpreted with the same model. However, the offset in flux among the models in KASCADE-Grande data is larger compared to the KASCADE ones. As the systematic uncertainties unrelated to the model are essentially common to all the three energy spectra, it is not straightforward to imagine that the offset of KASCADE-Grande with respect to KASCADE could be corrected commonly for the three models. As an example, the SIBYLL spectrum of KASCADE-Grande is already in excellent agreement with KASCADE, while QGSjet and EPOS produce a slight and

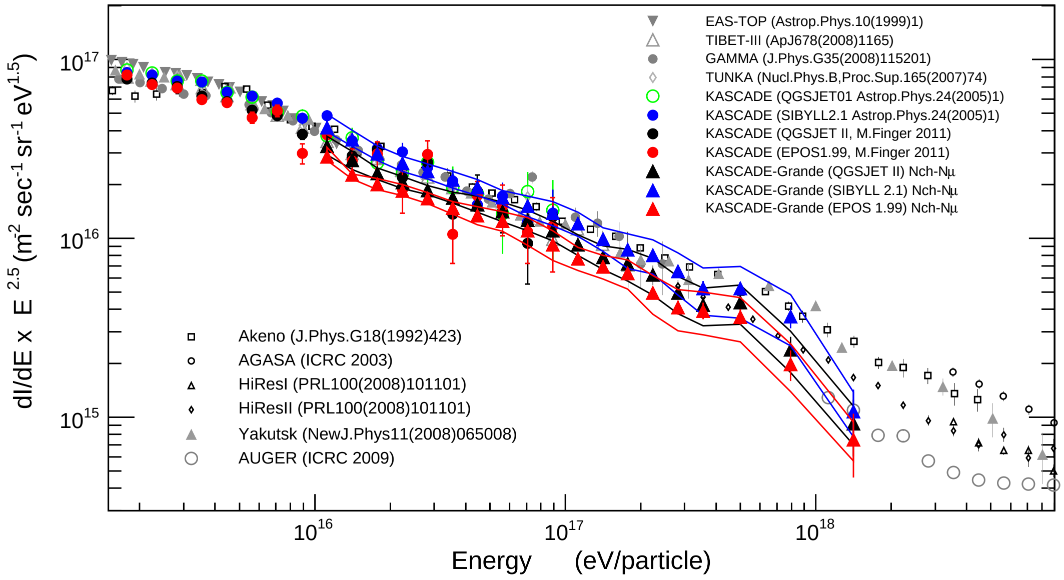

Figure 5: Comparison of the all-particle energy spectrum obtained with KASCADE-Grande data based on SIBYLL (blue), QGSJet (black), and EPOS (red) models to results of other experiments. The band denotes the systematic uncertainties in the flux estimation.

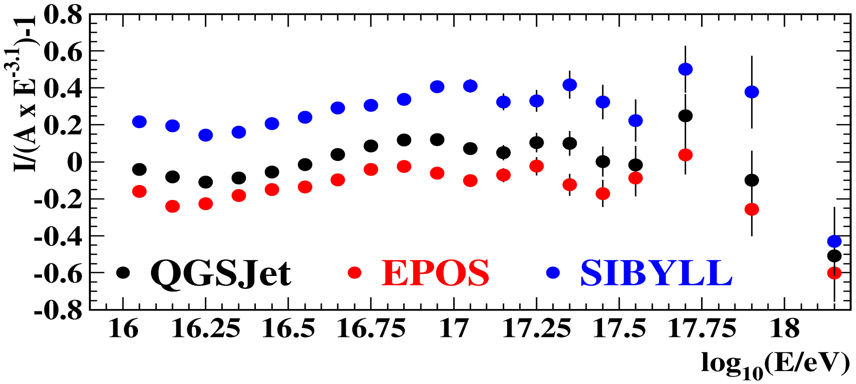

Figure 6: The residual flux after multiplying the spectrum with a factor of $E^{3.1}$ where A is the normalization factor for QGSjet. Blue dots refer to SIBYLL, black to QGSjet and red to EPOS.

Table 2: Differential flux values of the all-particle energy spectrum for SIBYLL and EPOS based analyses; for QGSjet see (W.D.Apel et al., 2012). The first column of errors denotes the statistical uncertainty, the second column the systematic one.

bin number	Energy [eV]	$dI/dE\pm$ stat. $\pm$ syst. $[m^{-2}s^{-1}sr^{-1}eV^{-1}]$ SIBYLL	$dI/dE\pm$ stat. $\pm$ syst. $[m^{-2}s^{-1}sr^{-1}eV^{-1}]$ EPOS
1	$1.11 \cdot 10^{16}$	$(3.13 \pm 0.02 \pm^{0.18}_{0.58}) \cdot 10^{-15}$	$(2.16 \pm 0.01 \pm^{0.11}_{0.26}) \cdot 10^{-15}$
2	$1.41 \cdot 10^{16}$	$(1.50 \pm 0.01 \pm^{0.13}_{0.18}) \cdot 10^{-15}$	$(9.55 \pm 0.06 \pm^{0.50}_{1.13}) \cdot 10^{-16}$
3	$1.78 \cdot 10^{16}$	$(7.06 \pm 0.04 \pm^{0.59}_{0.76}) \cdot 10^{-16}$	$(4.77 \pm 0.03 \pm^{0.32}_{0.35}) \cdot 10^{-16}$
4	$2.24 \cdot 10^{16}$	$(3.51 \pm 0.02 \pm^{0.35}_{0.31}) \cdot 10^{-16}$	$(2.47 \pm 0.02 \pm^{0.16}_{0.19}) \cdot 10^{-16}$
5	$2.82 \cdot 10^{16}$	$(1.78 \pm 0.01 \pm 0.17) \cdot 10^{-16}$	$(1.26 \pm 0.01 \pm 0.09) \cdot 10^{-16}$
6	$3.55 \cdot 10^{16}$	$(8.99 \pm 0.07 \pm 0.96) \cdot 10^{-17}$	$(6.25 \pm 0.06 \pm 0.52) \cdot 10^{-17}$
7	$4.47 \cdot 10^{16}$	$(4.58 \pm 0.05 \pm 0.48) \cdot 10^{-17}$	$(3.20 \pm 0.04 \pm 0.37) \cdot 10^{-17}$
8	$5.62 \cdot 10^{16}$	$(2.27 \pm 0.03 \pm 0.20) \cdot 10^{-17}$	$(1.67 \pm 0.03 \pm 0.21) \cdot 10^{-17}$
9	$7.08 \cdot 10^{16}$	$(1.14 \pm 0.02 \pm 0.15) \cdot 10^{-17}$	$(8.30 \pm 0.16 \pm 1.47) \cdot 10^{-18}$
10	$8.91 \cdot 10^{16}$	$(5.86 \pm 0.12 \pm 0.90) \cdot 10^{-18}$	$(3.91 \pm 0.10 \pm 0.73) \cdot 10^{-18}$
11	$1.12 \cdot 10^{17}$	$(2.88 \pm 0.07 \pm 0.45) \cdot 10^{-18}$	$(1.83 \pm 0.06 \pm 0.27) \cdot 10^{-18}$
12	$1.41 \cdot 10^{17}$	$(1.32 \pm 0.05 \pm 0.20) \cdot 10^{-18}$	$(9.28 \pm 0.38 \pm 1.38) \cdot 10^{-18}$
13	$1.78 \cdot 10^{17}$	$(6.51 \pm 0.28 \pm 1.43) \cdot 10^{-19}$	$(4.78 \pm 0.24 \pm 0.88) \cdot 10^{-19}$
14	$2.24 \cdot 10^{17}$	$(3.40 \pm 0.18 \pm 0.73) \cdot 10^{-19}$	$(2.10 \pm 0.14 \pm 0.51) \cdot 10^{-19}$
15	$2.82 \cdot 10^{17}$	$(1.55 \pm 0.11 \pm 0.41) \cdot 10^{-19}$	$(9.73 \pm 0.86 \pm 2.54) \cdot 10^{-19}$
16	$3.55 \cdot 10^{17}$	$(7.04 \pm 0.66 \pm 2.08) \cdot 10^{-20}$	$(5.25 \pm 0.57 \pm 1.41) \cdot 10^{-20}$
17	$5.01 \cdot 10^{17}$	$(2.96 \pm 0.25 \pm 0.95) \cdot 10^{-20}$	$(2.05 \pm 0.21 \pm 0.57) \cdot 10^{-20}$
18	$7.94 \cdot 10^{17}$	$(6.52 \pm 0.93 \pm 2.08) \cdot 10^{-21}$	$(3.52 \pm 0.68 \pm 1.04) \cdot 10^{-21}$
19	$1.41 \cdot 10^{18}$	$(4.53 \pm 1.47 \pm 1.26) \cdot 10^{-22}$	$(3.16 \pm 1.22 \pm 0.77) \cdot 10^{-22}$

more pronounced shift towards lower fluxes in KASCADE-Grande. Therefore, a readjustment of EPOS and QGSjet spectra would produce automatically a shift of the SIBYLL one. It should anyway be noticed that KASCADE data suffer from larger fluctuations, in particular when interpreted with the EPOS hadronic interaction model. One possible reason behind this systematic effect refers to the attenuation length in the atmosphere which would enhance the difference in case of KASCADE-Grande where showers up to 40° are considered, while KASCADE results are based on the measured data of only the first angular bin.

In order to quantify better the change of slopes of the spectrum, figure 7 shows the residuals of the all-particle energy spectrum multiplied by a factor in such a way that the middle part of the spectrum becomes flat. A power law index of $\gamma_1 = -2.972 \pm 0.020$ (-2.923 ± 0.023) is obtained by fitting the range of $\log_{10}(E/eV) = 16.3 - 17.0$ (16.2 - 16.9) in case of SIBYLL (EPOS). The concave spectrum just above 10^{16} eV is significant with respect to the systematic and statistical uncertainties. The effect is particularly evident in QGSjet and SIBYLL reconstructed spectra, and less pronounced in EPOS due to the energy shift of the data. In fact for all the three models the data

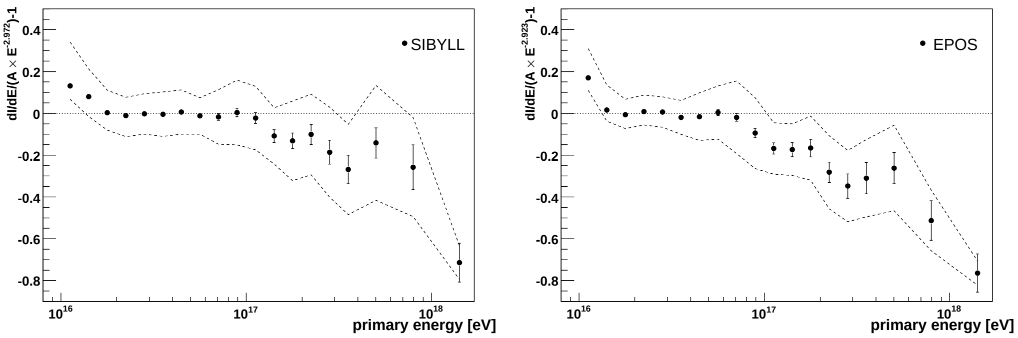

Figure 7: The all-particle energy spectrum obtained with KASCADE-Grande. The residual flux after multiplying the spectrum with a factor of $E^{2.972}(E^{2.923})$ in case of SIBYLL (EPOS) and normalized with A (a specific value for each interaction model) is displayed as well as the band of systematic uncertainty.

point at $1.11\cdot\ 10^{16}$ eV has a significance larger than $2\,\sigma$ if compared with the extrapolation of the power-law fit in the central part of the spectrum. This is a conservative result obtained by assuming that no correlation exists between the systematic uncertainties in near-by data points. A more careful study of such uncertainties and their bin-to-bin dependence indicates that the significance is indeed even higher and that in case of SIBYLL also the second point at $1.41{\cdot}10^{16}$ eV has a significance larger than $2\,\sigma$.
Another feature in the spectrum is a small break at around 10^{17} eV. Applying a second power law fit above 10^{17} eV an index of $\gamma_2 = -3.28 \pm 0.10$ ($\gamma = -3.30 \pm 0.07$) is obtained for SIBYLL (EPOS). Fitting the spectrum with a function of two power laws intercepted by a smooth knee the energy of the break is assigned to $\log_{10}(E/eV) = 17.03{\pm}0.13$ ($\log_{10}(E/eV) = 16.85{\pm}0.08$) in case of SIBYLL (EPOS).

4. The *k* parameter and the separation into mass groups

In the following we will discuss the origin of the steepening in the spectrum around 10^{17} eV in terms of mass-group separation. The threshold of the experiment is too high to repeat a similar study also for the concavity around 10^{16} eV. For this reason we focus now on the energy spectrum at energies $\log_{10}(E/eV) > 16.2$. The study is performed subdividing the measured data in two samples, defined as 'heavy' and 'light' mass-groups based on the k parameter - see equation 2.

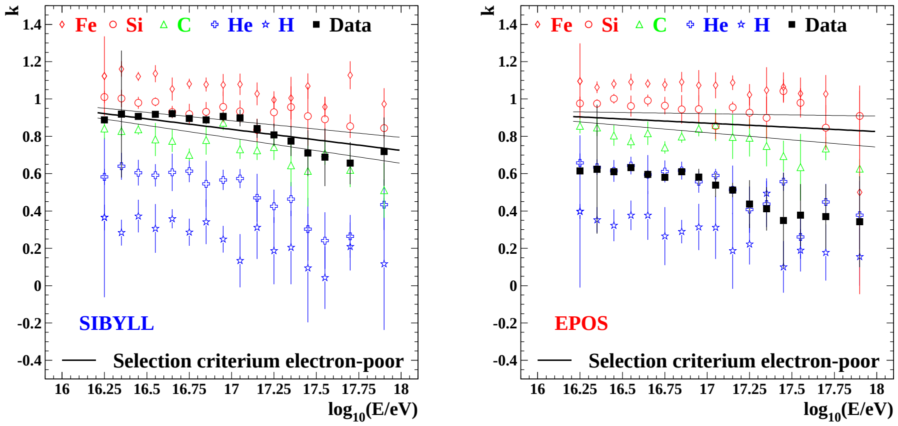

Figure 8: Evolution of the k parameter as a function of the reconstructed energy for experimental data compared with simulations of primary masses for the angular range 0-24°. SIBYLL results are displayed on the left plot, and EPOS results on the right one. The error bars include statistical as well as reconstruction uncertainties of k. The line displays the chosen energy dependent k values for separating the mass groups, where the thin lines assign the uncertainty of the selection.

Data from the first two angular bins are grouped together as well as for the last two angular bins to reduce the statistical uncertainties in the fitting procedures. As an example, fig. 8 shows the evolution of the k parameter as a function of the reconstructed energy for the first two zenith angle bins. A similar behavior is observed for all angular ranges. The error bars indicate the average dispersion of the k parameter among different bins, which include statistical errors, and systematic uncertainties derived from equations 1- 3. The width of the k distributions decreases slightly for increasing energy and amounts, at 10^{17} eV, to about ±0.2, ±0.15, ±0.4 for H, Fe, and experimental data, respectively. The same figure shows also the behavior of the simulated elements. In case of SIBYLL the average value of k for the experimental data is located between C and Si groups. It is almost constant in the range 10^{16} - 10^{17} eV, and it decreases at the highest energies. The simulated showers suffer from a lack of statistics at the highest energies. In fact, the mass groups of the simulated showers tend to give smaller k values at high energies. It has to be kept in mind that the k parameter has been defined to give values around 0 for H and around 1 for Fe when the events are expressed as a function of N_{ch} as shown in Appendix A and not as a function of energy. This explains the general shift of H from 0 and the fact that a dependence

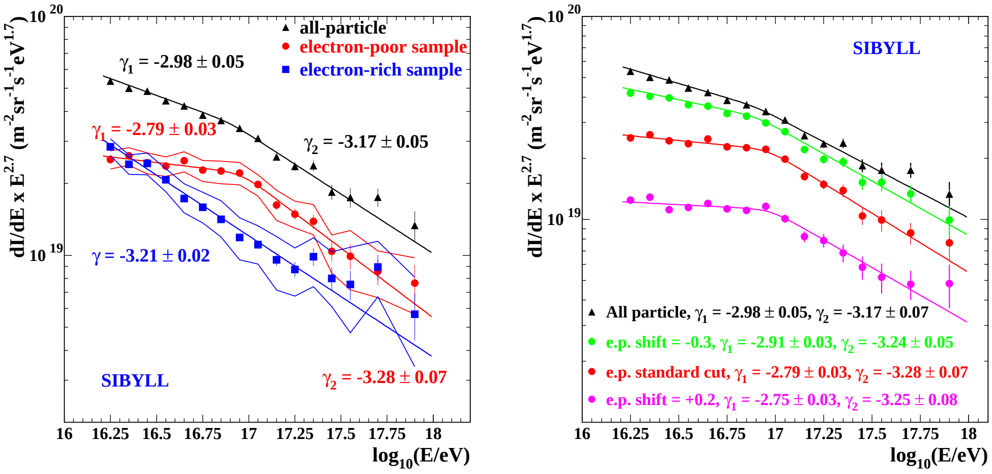

Figure 9: Left: Reconstructed energy spectrum of the heavy and light components together with the all-particle spectrum for the angular range $0° - 40°$ for the SIBYLL hadronic interaction model. The error bars show the statistical uncertainties; the bands assign systematic uncertainties due to the selection of subsamples. Fits on the spectra and resulting slopes are also indicated. Right: Energy spectra of heavy event samples obtained by different selection and reconstruction criteria. The original heavy spectrum of the left figure is compared with the spectra from a more selective and loose cut in the k parameter.

of k as a function of energy might exist.
The same trend exists in case of EPOS but the k values are centered around lighter primaries, namely He. This behavior can be ascribed to the different ratio N_{ch}/N_{μ} for the two models.

Fig. 8 shows also 3 straight lines. The thick solid line is used to separate events into heavy and light mass groups and it is defined by fitting the $k_h(E) = (k_{Si}(E) + k_C(E))/2$ points which are obtained by averaging the values of k for Si and C components. The two thin lines represent the uncertainties in defining this energy-dependent selection-cut. The assignment to the heavy or light mass groups is performed on an event-by-event basis. Naturally, the absolute abundances of the events in the two samples depend on the location of the straight lines. However, the evolution of the abundances as a function of energy will be retained by this approach, as the lines are defined through a fit to the k values. The resulting spec-

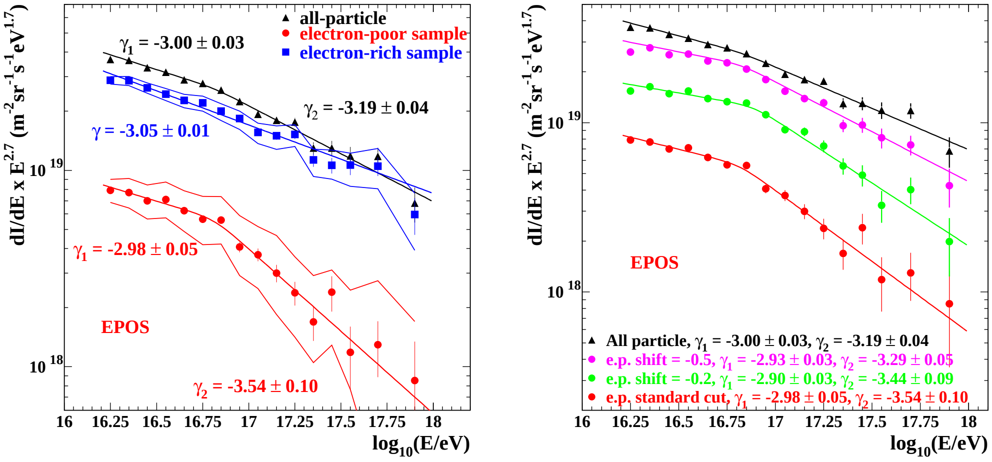

Figure 10: Same as fig.9 but for the EPOS hadronic interaction model. In the right-hand plot, the effect of two shifts in the k-cut by -0.2 and -0.5 are shown. The shift by -0.2 enhances the flux of the heavy component keeping the variation of the slope almost unchanged ($\Delta\gamma_{E,-0.2} \sim 0.54$ instead of $\Delta\gamma_{E,e.p} \sim 0.56$). With the shift by -0.5, the heavy component becomes contaminated by the light one and the knee-like feature is attenuated ($\Delta\gamma_{E,-0.5} \sim 0.36$) and approaches the one seen in the all-particle spectrum ($\Delta\gamma_{E,all} \sim 0.19$) .

tra are shown in the left panels of fig.9 and fig.10. With such a selection cut the reconstructed spectrum of the heavy primary sample shows a distinct knee-like feature around 10^{17} eV for both hadronic interaction models. Applying a fit of two power laws to the spectrum interconnected by a smooth knee in the entire energy range $16.2 < \log_{10}(E/eV) < 18.0$ results in a statistical significance of 7.4σ (4.0σ) for SIBYLL (EPOS) that the entire spectrum cannot be fitted with a single power-law. The change of the spectral slope is $\Delta\gamma = -0.49 \pm 0.08$ (-0.56 ± 0.11) from $\gamma_1 = -2.79 \pm 0.03$ (-2.98 ± 0.05) to $\gamma_2 = -3.28 \pm 0.07$ (-3.54 ± 0.10) with the break position at $\log_{10}(E/eV) = 16.96 \pm 0.04$ (16.82 ± 0.07). Applying the same function to the all-particle spectrum results in a statistical significance of only 2.7σ (2.8σ) that a fit of two power laws is needed to describe the spectrum. Here the change of the spectral slope is from $\gamma_1 = -2.98 \pm 0.05$ (-3.00 ± 0.03) to $\gamma_2 = -3.17 \pm 0.05$ (-3.19 ± 0.04), with the break position at $\log_{10}(E/eV) = 16.90 \pm 0.12$ (16.82 ± 0.09). Hence, the selection of heavy primaries enhances the knee-like feature that is already present in the all-particle spectrum. The slight difference in the position of the break reflects the difference in the energy assignment given to the experimental data by the two hadronic interaction models. The spectrum of the light component is compatible with a single power law with slope index $\gamma = -3.21 \pm 0.02$ (-3.05 ± 0.01), even though a change of slope cannot be excluded at the highest energies. These results, together with similar findings obtained with QGSjet (W.D.Apel et al., 2011), are summarized in table 3.

The error bands in fig.9 and fig.10 (left panels) show the uncertainty in the spectrum if the uncertainty on the selection cut is taken into account. In order to further validate the present result, parallel shifts of the cut-line on the heavy sample have been applied. Specifically, by shifting the cut line to higher values of k, the heavy component sample is enhanced, and its flux diminishes, while shifting the cut line towards lower values of k, the heavy sample becomes more contaminated by light events and the flux increases. The right-hand plots of fig.9 and fig.10 indicate that shifting up the line cut keeps the knee-like structure unchanged, while shifts down tend to smooth out the structure. In case of EPOS, because the flux of the heavy component is already very low, only cuts increasing the sample are applied. However, for a shift of the order of -0.2, the result is unchanged ($\Delta\gamma_{E,-0.2} \sim 0.54$ instead of $\Delta\gamma_{E,e.p.} \sim 0.56$ for the standard cut). Instead, a shift of the order of -0.5 tends to smooth out the knee-like feature ($\Delta\gamma_{E,-0.5} \sim 0.36$) in the direction of the all-particle spectrum ($\Delta\gamma_{E,all} \sim 0.19$). It is important to underline the difference between the light sample of the left-hand panel of fig.10 with the heavy sample in the right-hand panel of fig.10 with a -0.5 shift in the k parameter. Both correspond to a similar flux, however, the sample on the left contains the light component and a possible contamination from the heavy one. The right one contains the heavy component and a possible contamination from the light one. This explains the difference in the shape of the spectrum.

The shift in SIBYLL by +0.2 selects approximately the same fraction of heavy events as for the standard cuts in EPOS ($\sim 20\,\%$ around $10^{16.25}$ eV) and the change of slope is similar to EPOS ($\Delta\gamma_{S,+0.2} \sim 0.50$). This comparison holds also for the other two cases. The standard cuts in SIBYLL select $\sim 50\,\%$ of the events around $10^{16.25}$ eV as for the -0.2 shift in EPOS, and give a similar result: $\Delta\gamma_{S,e.p.} \sim 0.49$. The loose cut of -0.3 in SIBYLL selects $\sim 80\,\%$ of the events around $10^{16.25}$ eV as heavy just as for EPOS using -0.5. Also in this case $\Delta\gamma_{S,+0.5} \sim 0.33$ is quite similar to EPOS. All the above checks confirm

Table 3: Slope of the different spectra and break positions obtained with the three different hadronic interaction models, by applying the k parameter analysis in order to separate the spectra into different mass groups. QGSjet results are from (W.D.Apel et al., 2011).

Model	EPOS	QGSjet	SIBYLL
All-particle			
γ_1	-3.00 ± 0.03	-2.95 ± 0.05	-2.98 ± 0.05
γ_2	-3.19 ± 0.04	-3.24 ± 0.08	-3.17 ± 0.05
$\log_{10}(E/eV)$	16.82 ± 0.09	16.92 ± 0.10	16.90 ± 0.12
significance (σ)	2.8	2.1	2.7
Heavy component			
γ_1	-2.98 ± 0.05	-2.76 ± 0.02	-2.79 ± 0.03
γ_2	-3.54 ± 0.10	-3.24 ± 0.05	-3.28 ± 0.07
$\log_{10}(E/eV)$	16.82 ± 0.07	16.92 ± 0.04	16.96 ± 0.04
significance (σ)	4.0	3.5	7.4
Light component			
γ	-3.05 ± 0.01	-3.18 ± 0.01	-3.21 ± 0.02

that the structure seen in the spectrum is caused by the heavy component, and that the conclusion is essentially independent of the particular hadronic interaction model used in the analysis.

In case of QGSjet further independent analyses have been conducted and presented in (W.D.Apel et al., 2011) and they support this conclusion.

5. Conclusions

The energy spectrum and separation into mass-groups have been obtained for the SIBYLL and EPOS hadronic interaction models using the same approach defined for QGSjet in (W.D.Apel et al., 2011, 2012). The obtained results confirm qualitatively the previous findings. The all-particle spectrum in the range 10^{16} - 10^{18} eV is found to exhibit some smaller structures: In particular, a hardening of the spectrum is observed at 2×10^{16} eV and a small break-off at around 8×10^{16} eV. The energy position of such features slightly depends on the energy assigned by the interaction model to the event. In general the position of the structures is at lower energies for EPOS and higher energies for SIBYLL.

The separation into mass groups performed via the k parameter reveals that the knee-like feature around 10^{17} eV in the all-particle spectrum is associated with a break in the heavy component. However, in case of EPOS the break holds also for a less tight cut on what is defined as heavy component. In this sense the interpretation of which mass group is responsible for this break strongly depends on the hadronic interaction model employed to interpret the data.

The all-particle spectra obtained by KASCADE-Grande are in general in good agreement with the spectra obtained by KASCADE, even though the systematic uncertainty is slightly larger in case of KASCADE-Grande.

Acknowledgments

The authors would like to thank the members of the engineering and technical staff of the KASCADE-Grande collaboration, who contributed to the success of the experiment. The KASCADE-Grande experiment is supported by the BMBF of Germany, the MIUR and INAF of Italy, the Polish Ministry of Science and Higher Education, and the Romanian Authority for Scientific Research UEFISCDI (PNII-IDEI grants 271/2011 and 17/2011). J.C.A.V acknowledges the partial support of CONACyT and the DAA-Proalmex program (2009-2012). The present study is supported by the 'Helmholtz Alliance for Astroparticle Physics - HAP' funded by the Initiative and Networking Fund of the Helmholtz Association, Germany.

Appendix A. Calibration Functions and k parameter

The coefficients a, b, c, d of equations 1-3 are obtained by simulating H and Fe primaries independently for each zenith angular range, where fits are applied to the scatter plots $(N_{ch}, N_{ch}/N_{\mu})$ and (N_{ch}, E_0). The fit range is chosen to be $6 \leq \log_{10}(N_{ch}) \leq 8$, i.e. in a region where 100% trigger efficiency is guaranteed. Primary protons exhibit larger fluctuations than heavier primaries, therefore the coefficients c and d are obtained iteratively, choosing the best combination of values, inside the uncertainties of the parameters, which better reproduce the simulated energy spectrum. As an example, Figs. A.11 and A.12 show the scatter plots including the resulting functions for the first angular bin obtained for SIBYLL and EPOS simulated showers, respectively. Shown are the errors on the mean, which are small due to the large Monte Carlo statistics. For the fits, however, we also take into account the width of the distribution in order to avoid a bias due to varying shower-to-shower fluctuations, in particular, in case of primary protons at small shower sizes. The average values take into account the weighting factor applied to the individual events in order to reproduce a spectrum with γ = -3. The distributions of the individual events in the plots (small dots) do not take

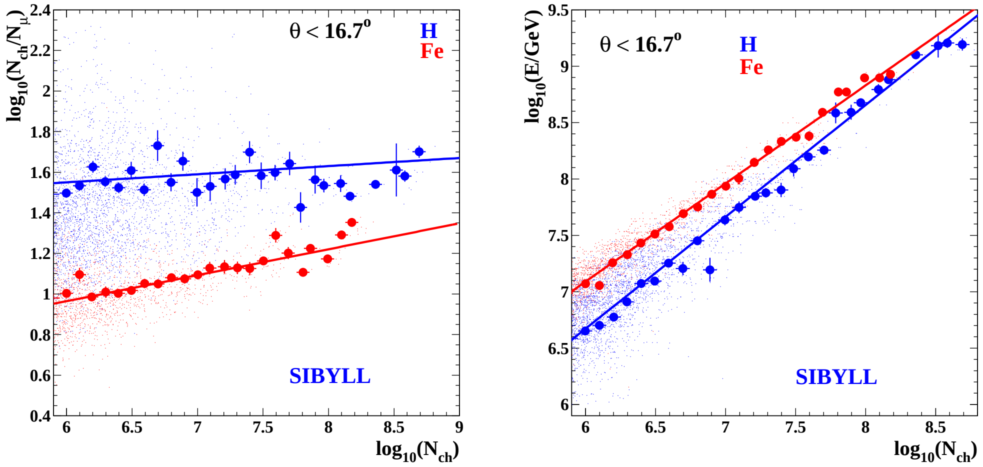

Figure A.11: SIBYLL calibration functions. Left panel: Scatter plot of the reconstructed N_{ch}/N_{μ} vs. N_{ch} for primary iron and proton nuclei, and for the first angular bin. The full dots and error bars indicate the mean and statistical errors on the mean of the distribution of the individual events (small dots). The fits result in parameters c and d of expression 3. Right panel: Scatter plots of E vs. N_{ch} for iron and proton primary nuclei. The fits result in parameters a and b of expression 1.

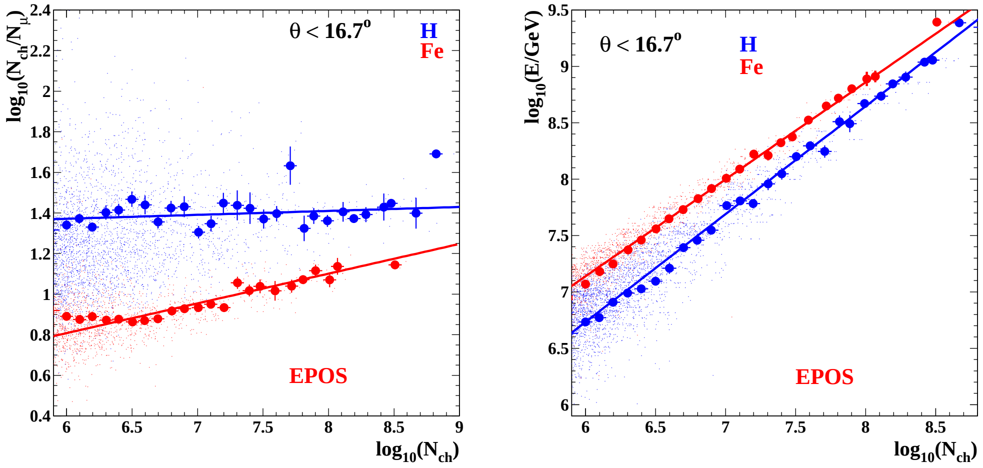

Figure A.12: EPOS calibration functions for the first angular bin. See caption of figure A.11 for explanations.

into account this effect, as they are only meant to show the width. For this reason they are not necessarily centered on the corresponding average values.

It is obvious that taking into account the correlation of the observables will significantly reduce the composition dependence of the energy assignment. Similar procedures are applied to the other angular bins, and all coefficients are compiled in Table A.4. The uncertainties of these numbers are small. Still they are considered in the calculation of the total systematic uncertainty.

Fig. A.13 shows the capability of reproducing simulated energy spectra. A mixture of light (H and He), heavy (Si and Fe) in both cases with 50% abundance for each element, and one of 5 different primaries with 20% abundance each are shown as examples for SIBYLL. The true flux is always reproduced within 10% uncertainty, except at the highest energies where the statistical uncertainties dominate. No response matrix to account for bin to bin fluctuations is applied yet, however, the result is already quite satisfactory. This is important because the separation of 'heavy' and 'light' mass groups is based on an event by event basis, therefore, it is important that the calibration functions reproduce properly the simulated energy spectrum. The right-hand side of fig.A.13 shows also the relative uncertainty in the energy assignment on an event-by-event basis for simulated showers using a mixture of all primaries, as well as H and Fe, divided in bins of true energy (E_{true}). The small offset in the mean values of the distributions at low energies is necessary to take into account the effect of shower fluctuations on a steep spectrum. Such an offset does not appear in the left panel of the figure, which indicates that the correct energy spectrum is well reproduced. Results for

Table A.4: Coefficients of the energy calibration functions for SIBYLL and EPOS simulated showers.

Angular bin	a		b		c		d	
SIBYLL	H	Fe	H	Fe	H	Fe	H	Fe
$\Theta < 16.7°$	0.99	0.87	0.72	1.87	0.04	0.13	1.31	0.20
$16.7° \leq \Theta < 24.0°$	0.95	0.87	1.12	1.97	0.04	0.13	1.17	0.11
$24.0° \leq \Theta < 29.9°$	0.94	0.92	1.25	1.75	0.05	0.12	1.06	0.11
$29.9° \leq \Theta < 35.1°$	0.95	0.91	1.37	1.94	0.05	0.13	0.93	-0.09
$35.1° \leq \Theta < 40.0°$	0.90	0.89	1.86	2.24	0.06	0.14	0.77	-0.25
EPOS	H	Fe	H	Fe	H	Fe	H	Fe
$\Theta < 16.7°$	0.96	0.86	0.99	1.98	0.02	0.15	1.26	-0.07
$16.7° \leq \Theta < 24.0°$	0.89	0.89	1.53	1.87	0.11	0.11	0.54	0.09
$24.0° \leq \Theta < 29.9°$	0.90	0.92	1.56	1.80	0.13	0.10	0.34	0.10
$29.9° \leq \Theta < 35.1°$	0.90	0.88	1.67	2.14	0.14	0.12	0.25	-0.10
$35.1° \leq \Theta < 40.0°$	0.90	0.90	1.87	2.14	0.13	0.12	0.22	-0.18

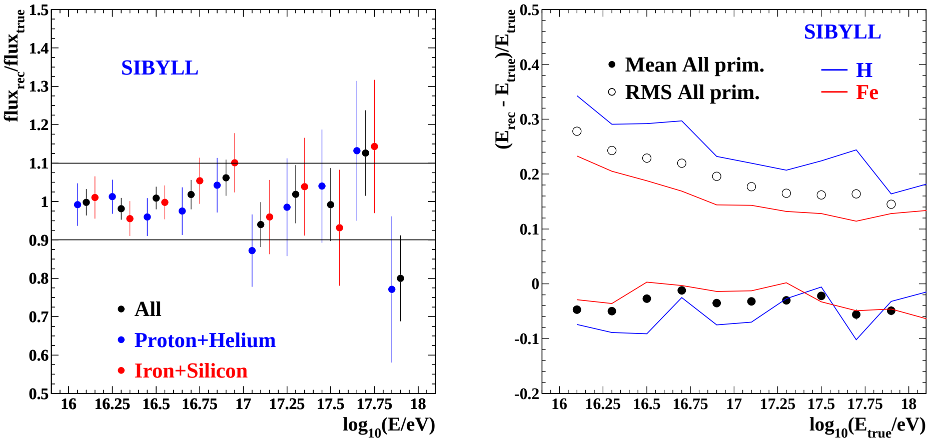

Figure A.13: Left: Ratio between the reconstructed and true simulated energy spectrum for light (blue), heavy (red) and all mixed primaries (black) summing up all angular bins. No response matrix is applied yet to the simulated showers. Similar results are obtained also in case of EPOS. Right: Resolution in the energy assignment for a mixture of primaries of the 5 simulated mass groups (relative abundance of each group 20%), for H and Fe. The full dots show the offset of the reconstructed energy E_{rec} in bins of true energy E_{true}. The open dots show the RMS of such distributions. Results refer to SIBYLL simulated showers, but similar conclusions are drawn for EPOS as well.

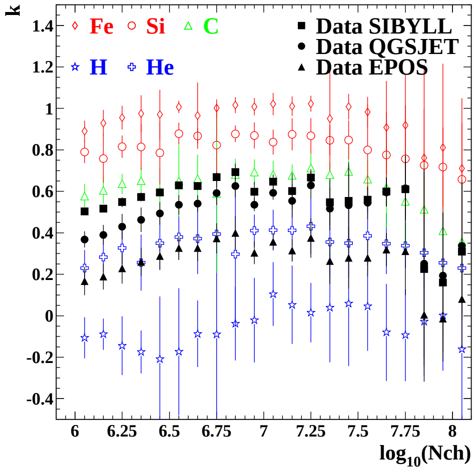

Figure A.14: Evolution of the k parameter as a function of N_{ch} for experimental data compared with pure primary spectra for the entire angular range 0-40°.

pure H and Fe primaries are also shown by lines. Naturally, H suffers from higher fluctuations and the offset is also more pronounced. Similar results are obtained also in case of EPOS.
Fig. A.14 shows, after averaging all angular bins, the evolution of the k parameter as a function of N_{ch} of the experimental data, for the three hadronic interaction models. The average behavior, among the three hadronic interaction models, of the k parameter for simulated showers (pure H, He, C, Si, Fe primary spectra), is also shown for comparison. A similar behavior is obtained if each angular bin is analyzed separately. The error bars indicate the average dispersion of the k parameter for different bins, which include statistical errors, and systematic uncertainties as derived from equation 3 for each angular bin. The result that can be derived from fig. A.14, is that QGSjet and SIBYLL tend to give a composition heavier than EPOS. More information can be extracted looking at the same plot as a function of energy.

Appendix B. Unfolding of the energy spectrum

As the fluctuations in the energy determination are larger than the bin size of the aimed-for energy spectrum an unfolding procedure is applied, briefly explained in the following, while more details can be found in (W.D.Apel et al., 2012). Using Monte Carlo simulations a response matrix R_{ij} is constructed for the energy interval $\log_{10}(E/\mathrm{GeV}) = 6 - 9.5$, i.e. covering the entire range where fluctuations can affect the energy spectrum. This matrix represents the conditional probability $P(E_j|E_j^{true})$, of an event with true energy in bin $\log_{10}(E_j^{true})$ being reconstructed with energy $\log_{10}(E_j)$. By means of the response matrix a system of simultaneous equations, $n_j^{exp} = \sum_{i=1}^{N} P(E_j|E_j^{true})n_i^{true}$, is established between the distribution of measured events, n_i^{exp} and the actual energy distribution, n_j^{true}. The system is solved by means of the Bayes-algorithm (G.D.Agostini, 1995). To avoid the problem of having wild fluctuations when increasing the number of iterations in the procedure a moderate regularization method is applied, consisting of smoothing the result of unfolding in a given step before using it in the next iteration. For the response matrix, quadratic fits along the diagonals are performed in the region of full efficiency to interpolate data into the region of low statistics. It is worth to mention that among several tests employed to verify the performance of the methods, it was checked that the algorithms do not produce artificial structures in the spectrum or hide peaks which could be significantly present in the data. In addition, tests have been performed to check for the consistency between the forward-folded and measured distributions. These tests were done in a similar way as for the other KASCADE and KASCADE-Grande studies ((T.Antoni et al. , 2005; W.D.Apel et al., 2013)).

In order to check that the unfolding procedure works properly, the ratio between unfolded and original simulated spectra is checked as already done for the raw data as shown in Fig. A.13. Also in fig. B.15 the true flux is always reproduced within 10% uncertainty. Fig. B.16 shows the flux obtained on the experimental data for all the 5 angular bins applying directly the calibration functions, as well as the unfolding. The spectra are artificially scaled to better show the differences between direct and unfolded spectra. In general, they are in satisfactory agreeement (of the order of a few percent). This indicates that for the mass group analysis, as it requires a decision on an event-by-event basis, the raw spectra provide already a quite accurate solution. However, in the case of the energy spectrum analysis, the unfolded ones are preferred.

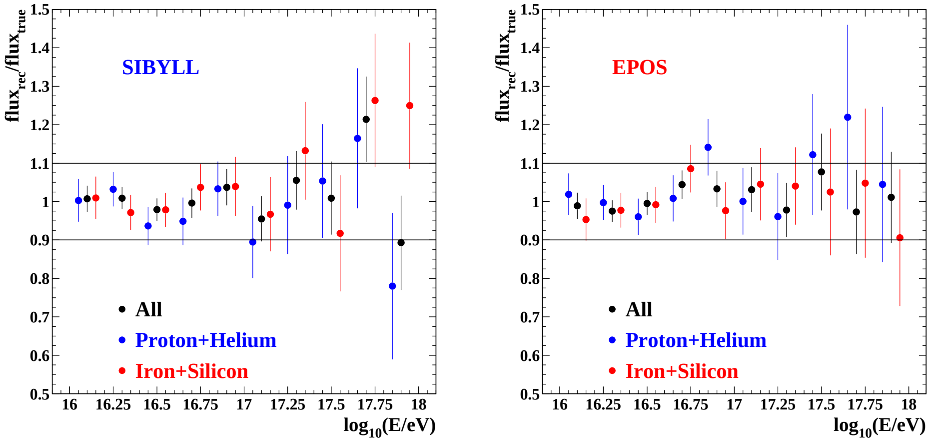

Figure B.15: Ratio between the unfolded and true simulated energy spectrum for light (blue), heavy (red) and all mixed primaries (black) summing up all angular bins. Left side is for SIBYLL while right side in EPOS case.

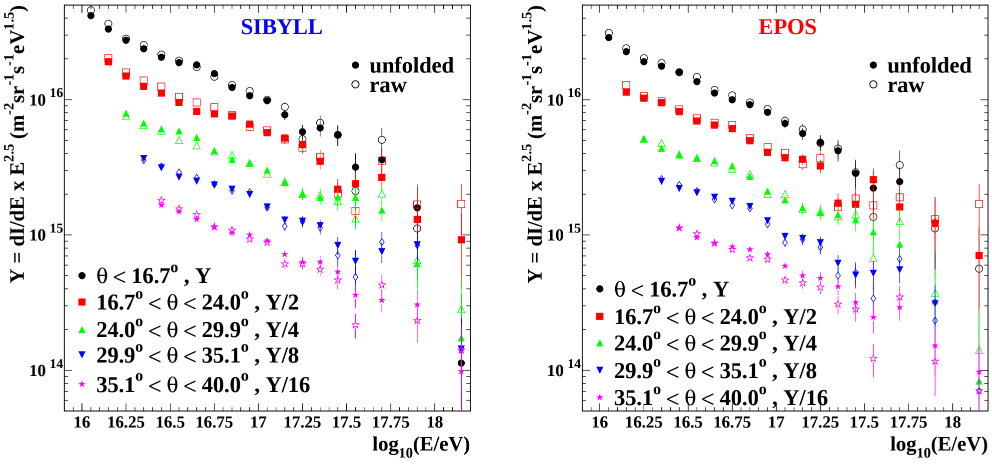

Figure B.16: Reconstructed all-particle energy spectra for all five angular bins. The directly reconstructed, as well as the unfolded spectra, are displayed, where the spectra are scaled for better visibility (left-hand panel SIBYLL, right-hand panel EPOS). Only statistical errors are displayed.

References

Aglietta, M., Alessandro, B., Antonioli P., et al. (EAS-TOP & MACRO Coll.), The cosmic ray primary composition between 10^{15} and 10^{16} eV from Extensive Air Showers electromagnetic and TeV muon data, Astrop. Phys. 20, 641-652, 2004.

Aglietta, M., Alessandro, B., Antonioli P., et al. (EAS-TOP Coll.), The cosmic ray primary composition in the 'knee' region through the EAS electromagnetic and muon measurements at EAS-TOP, Astrop. Phys. 21, 583-596, 2004.

Agostini, G.D., A multidimensional unfolding method based on Bayes- theorem, Nucl. Instr. & Meth. A 362, 487-498, 1995.

Antoni, T., Apel, W.D., Badea A.F., et al. (KASCADE Coll.), KASCADE measurements of energy spectra for elemental groups of cosmic rays: Results and open problems, Astrop. Phys. 24, 1-25, 2005.

Apel, W.D., Arteaga, J.C., Badea, A.F., et al. (KASCADE-Grande Coll.), The KASCADE-Grande Experiment, Nucl. Instr. & Meth. A 620, 202-216, 2010.

Apel, W.D., Arteaga-Velázquez, J.C., Bekk, K., et al. (KASCADE-Grande Coll.), Kneelike Structure in the Spectrum of the Heavy Component of Cosmic Rays Observed with KASCADE-Grande, Phys. Rev. Lett. 107, 171104/1-5, 2011.

Apel, W.D., Arteaga-Velázquez, J.C., Bekk, K., et al. (KASCADE-Grande Coll.), The spectrum of high-energy cosmic rays measured with KASCADE-Grande, Astrop. Phys. 36, 183-194, 2012.

Apel, W.D., Arteaga-Velázquez, J.C., Bekk, K., et al. (KASCADE-Grande Coll.), KASCADE-Grande measurements of energy spectra for elemental groups of cosmic rays, submitted to Astroparticle Physics.

Arteaga-Velázquez, J.C., Apel, W.D., Bekk, K., et al. (KASCADE-Grande Coll.), Test of Hadronic Interaction Models with the KASCADE-Grande muon data, to be published on Proc. of ISVHECRI 2012.

Battistoni, G., Cerutti, F., Fassò, A., et al., The FLUKA code: Description and benchmarking, AIP Conference Proceedings 896, 31-49, 2007.

Berezinsky, V., Gazizov, A., Grigorieva, S., On astrophysical solution to ultrahigh energy cosmic rays, Phys. Rev. D74/4, 043005/1-35, 2006.

Bertaina, M., Apel, W.D., Arteaga-Velázquez, J.C., et al. (KASCADE-Grande Coll.), The cosmic ray energy spectrum in the range 10^{16} - 10^{18} eV measured by KASCADE-Grande, Astrophys. Space Sci. Trans. 7, 229-234, 2011.

De Donato, C., Medina-Tanco, Experimental constraints on the astrophysical interpretation of the cosmic ray Galactic-extragalactic transition region, Astrop. Phys. 32, 253-268, 2009.

Engel, J., Gaisser, T.K., Lipari, P., et al., Nucleus-nucleus collisions and interpretation of cosmic-ray cascades, Phys. Rev. D 46, 5013-5025, 1992.

Heck, D., Knapp, J., Capdevielle, J., et al., CORSIKA: A Monte Carlo Code to Simulate Extensive Air Showers, Forschungszentrum Karlsruhe Internal Report FZKA6019, 1998.

Hillas, A.M., Can diffusive shock acceleration in supernova remnants account for high-energy galactic cosmic rays?, J. Phys. G: Nucl. Part. Phys. 31, R95-R131, 2005.

Hörandel, J.R., Models of the knee in the energy spectrum of cosmic rays, Astrop. Phys. 21, 241-265, 2004.

Lagutin A.A., Raikin, R.I., Lateral distribution of electrons in EAS at superhigh energies: predictions and experimental data, Nucl. Phys. B - Proc. Suppl. 97, 274-277, 2001.

Ostapchenko, S., Nonlinear screening effects in high energy hadronic interactions, Phys. Rev. D 74, 014026/1-17, 2006.

Peters, B., Primary Cosmic Radiation and Extensive Air Showers, Nuovo Cimento, 22, 800-819, 1961.

Werner, K., Liu, F.M., Pierog, T., Parton ladder splitting and the rapidity dependence of tranverse momentum spectra in deuteron-gold collisions at BNL Relativistic Heavy Ion Collider, Phys. Rev. C 74, 044902/1-11, 2006.